Chinese Chemical Letters 34 (2023) 108810

Contents lists available at ScienceDirect

Chinese Chemical Letters

journal homepage: www.elsevier.com/locate/cclet

Trace doping realizing superior electrochemical performance in P2-type $Na_{0.50}Li_{0.08}Mn_{0.60}Co_{0.16}Ni_{0.16}O_2$ cathode for sodium-ion batteries

Hongying Hou[a,1], Jinxu Qiu[a,b,1], Bao Li[b], Liang Wang[b], Zhuangzhuang Zhang[b], Mengmin Jia[b], Xiaobing Lai[b], Mingming Han[b], Pengyao Yan[b], Dai-Huo Liu[b,*], Dongmei Dai[b,*], Bao Wang[c,*]

[a] Faculty of Material Science and Engineering, Kunming University of Science and Technology, Kunming 650093 China
[b] Collaborative Innovation Center of Henan Province for Green Manufacturing of Fine Chemicals, Key Laboratory of Green Chemical Media and Reactions, Ministry of Education, School of Chemistry and Chemical Engineering, Henan Normal University, Xinxiang 453007, China
[c] State Key Laboratory of Biochemical Engineering, Institute of Process Engineering, Chinese Academy of Sciences, Beijing 100190, China

ARTICLE INFO

Article history:
Received 29 April 2023
Revised 1 June 2023
Accepted 12 July 2023
Available online 14 July 2023

Keywords:
P2-type layered oxide
Same-period elements doping
Rietveld refinement
Operando XRD
Sodium-ion battery

ABSTRACT

P2-type layered oxides are receiving significant interest due to their superior structure and intrinsic performances. There are strenuous attempts to balance the structure stability, phase transition as well as desirable electrochemical performances by inducing anion/cation ions, changing morphology, adjusting valence, *etc.* In this work, several same-period elements of Sc, Ti, V, Cr, Fe, Cu and Zn are doped into $Na_{0.50}Li_{0.08}Mn_{0.60}Co_{0.16}Ni_{0.16}O_2$ cathodes, which are manipulated by ions radii and valence state, further studied by operando X-ray powder diffraction patterns (XRD). As a result, the Cu^{2+} doped cathode performed higher rate capacities (as high as 86 mAh/g even at 10 C) and more stable structures (capacity retention of ~89.4% for 100 cycles), which owing to the synergistic effect among the tightened TMO_2 layer, enlarged *d*-spacing, reduce O–O electrostatic repulsion, ameliorate lattice distortion as well as mitigate ordering of Na^+/vacancy.

With the significant demand for rechargeable and clean-electrical energy storage, sodium-ion batteries (SIBs) are emerging as an alternative resource candidate to the grid, electric vehicles, and portable electronic devices because of their abundance, low cost as well as reliable sources [1–5]. The layered structures of Na_xTMO_2 (TM = consisting of one or more 3d orbital transition metal) are commonly made up of edge-sharing TMO_6 octahedra and sodium atoms with different sites, which can be mainly divided into P2-type and O3-type according to the local surroundings of Na^+ (the prismatic or octahedral), stacking sequence of nonequivalent TMO_2 slabs, and difference of oxygen atoms [6,7]. P2-type oxides usually yield faster Na^+ conductivity, high power density as well as good rate performances. Among them, manganese-based P2-type oxides also have attracted enormous attention due to their satisfactory electrochemical performance, low cost, and nontoxicity cathode systems for SIBs. Indelibly, influenced by Na^+/vacancy ordering and gliding of the TMO_2 slabs, irreversible phase transitions were induced upon Na^+ intercalation/deintercalation during the subsequent cycling. Slab gliding gratifies energetic balance, as increasing extraction of Na^+, therefore arising octahedral vacancies and decreased interlayer spacing, forming the stacked fault OP4 (described as "Z" phase) or O2 phase [8,9]. Moreover, the notorious tetragonal Jahn-Teller distortion lowers the energy of a system by certain bond length distortions to break the local crystal symmetry and lift the degeneracy of the electronic system [10]. In which high spin Mn^{3+} ($t_{2g}^3e_g^1$) inspires disproportionation from soluble Mn^{2+} and mutating of electrostatic interactions in adjoining atoms also leading to the grievous irreversible attenuation of capacity [11,12].

Therefore, various perspectives have been devoted to the design of modification methods with enlarged structures, tailoring morphology, restraining vacancy ordering, complementary cations valence states, tuning sodium occupancy sites, and even theoretical predictions, *etc.* [13–21]. On the purpose of relieving volume changes and catering proper Na^+ diffusion paths, a shale-liked

* Corresponding authors.
E-mail addresses: liudaihuo@htu.edu.cn (D.-H. Liu), daidongmei@htu.edu.cn (D. Dai), baowang@ipe.ac.cn (B. Wang).
[1] These authors contributed equally to this work.

https://doi.org/10.1016/j.cclet.2023.108810
1001-8417/

$Na_{0.67}MnO_2$ *via* expanding the Na^+ layer spacings to achieve near-zero-strain, which delivered a capacity of 95 mAh/g at 960 mA/g within the voltage range of 2.0–4.0 V [22]. Another strategy is to regulate the uniform distribution of Na^+ in favor of P2-type $Na_{2/3}Mn_{1/2}Ni_{1/6}Co_{1/3}O_2$ cathode with the ultralow volume change of 1.9% in the voltage of 1.5–4.5 V [23]. Oxygen-redox chemistry and bulk oxygen vacancies also could effectively relieve the loss of O^{2-}/O^{n-} redox and create Mn domains to resist the Jahn-Teller distortion [24,25]. Furthermore, ions substitution with various valence states and ion radii act as the pillars to support the robust framework among slabs. Such as redox active metal Ag^+, Fe^{3+}, Ce^{4+}, Nb^{5+}, Mo^{6+} as well as the electrochemical inert elements of Li^+, Mg^{2+}, Ca^{2+}, Al^{3+}, Si^{4+}, F^-, B^- and lanthanide, *etc.* They are also contributing to disrupting Na^+/vacancy ordering, enlarging channels of Na^+ migration, and efficaciously alleviation structure distortion, which is responsible for the improvement of electrochemical performances [26–39].

Although ions substitute has been intensively investigated, where the contrast of the doped elements tends to be one or two types and chemical components also show differences. It should be pointed out that the different radii and valences render different performances. The TM elements of the subgroup of 3d orbital (*e.g.*, *Sc*, Ti, V, Cr, Mn, Fe, Co, Ni, Cu and Zn elements) with the same outer electronic configuration and a different number of electrons are possessed electrochemically active in layered oxides. Wherein, 3d orbital elements also have similar ionic radii and different redox potentials that could renew the TMO_2 slabs avoiding Jahn-Teller distortion and ordering of Na^+/vacancy resulting in structural collapse. In addition, considering that doped Sc^{3+} has not been reported in SIBs, the counterparts of the $LiNi_{0.5}Mn_{1.5}O_4$ electrode were confirmed to enhance Li^+ diffusion kinetics [40]. The foreign ions decided on local structure rather than all regions and guided by these, the effect mechanism between the doped element and structure evolving need to be clarified, which could be beneficial for the selection of doped ions of P2-type to come up with a robust skeleton and fulfill higher energy density [41].

Herein, P2-type $Na_{0.50}Li_{0.08}Mn_{0.60}Co_{0.16}Ni_{0.16}O_2$ was adopted as a matrix material to study the impact of the changes of systematically doping Sc, Ti, V, Cr, Fe, Cu and Zn elements in the cathode materials. The strategy of compressing TM layered while broadening sodium layered in P2-type cathode materials could model a robust structure and expedite diffusion kinetics, indicating the smoothing processes of Na^+ during the charge/discharge as well as improved electrochemical performance. Besides, the Rietveld refinements help to verify the hypothesis, in which the synergistic effect between the TMO_2 layer and d-spacing could enhance the structural stability and promote Na^+ migration. Moreover, $NCMSc_{0.02}$, $NCMFe_{0.02,}$ and $NCMCu_{0.02}$ electrodes suffer from reversible structure evolutions, which are reflected in the slight shift of (002), (004), (101), (106) as well as (012) diffraction peaks.

The element quantitative analysis was confirmed by ICP-OES measurement for sintered samples listed in Table S1 (Supporting information), corresponding results of element composition are both consistent with the target designs. The powder XRD pattern of the precursor is shown in Fig. S1a (Supporting information), which is consistent with the Bragg positions for Mn_3O_4, Co_3O_4, $Ni(OH)_2$, $Mn(OH)_2$ and $Co(OH)_2$. Similarly, the sintered samples of NCM, $NCMSc_{0.02}$, $NCMTi_{0.02}$, $NCMV_{0.02}$, $NCMCr_{0.02}$, $NCMFe_{0.02}$ and $NCMZn_{0.02}$ are compared under the normalized method (Fig. S1b in Supporting information), confirming that all samples can be indexed into a major phase of the layered P2-type structure with P63/mmc (PDF#54–0894) space group. In detail, some additional Bragg peaks are arising from the superstructure due to the Na^+/vacancy ordering, and the split peak is related to the appearance of the symmetry structure of the orthorhombic (with Pnma space group), as marked by stars and rounds separately, which also has two kinds of Na positions (share faces or edges), but provided fewer Na^+ active sites than P2-type, specifically, the trigonal prism shares edges with TMO_6 is preferred for a broad range of Na contents (schematic of the crystal structure is shown in Fig. S2 in Supporting information) [42]. The cell parameters are further calculated by the GSAS software package (Fig. 1) [43,44]. From the structure refinements in Table S2 (Supporting information), the lattice parameters a/b, c, and V of doped samples are changed with various radii and valences comparing the prototype material of NCM ($a = b = 2.85541$ Å, $c = 11.20723$ Å and $V = 79.1347$ Å^3), affirming that the doped ions are successfully integrated into the crystal structure (Fig. 1i).

The long-term cycling durability and rate performances are conducted to evaluate the positive electrode materials. The radius of seven ions is ranked as follows: $Cr^{6+} < V^{4+} < Ti^{4+} < Fe^{3+} < Cu^{2+} < Zn^{2+} < Sc^{3+}$, while Figs. 2a and b show that the reversible discharge capacity of NCM, $NCMSc_{0.02}$, $NCMTi_{0.02}$, $NCMV_{0.02}$, $NCMCr_{0.02}$, $NCMFe_{0.02}$, $NCMCu_{0.02}$ and $NCMZn_{0.02}$ are 108, 104, 116, 86, 63, 112, 116 and 101 mAh/g at 0.5 C for 100 cycles, corresponding to the capacity retentions of ~84.2%, ~82.0%, ~85.9%, ~73.5%, ~56.3%, ~86.7%, ~89.4%, and ~85.5%, even the average discharge capacity are 49, 82, 78, 64, 10, 72, 86 and 82 mAh/g at 10 C, respectively. It should be noted that nearly all the composite phase exhibits fewer discharge capacities than the single P2-phase except for titanium doped, which is due to the decreased active sites in the orthorhombic phase. Whereas titanium doped could suppress the irreversible multiphase transformation accompanied by voltage increase by enlarging interslab distance, thus delivering higher reversible capacity for 100 cycles [45]. Conversely, the atomic coordination changed owing to the introduced chromium and vanadium ions, which higher valence and smaller radii than the matrix structure decided the local atomic distribution inclined to crystal lattice distortion. To meet potential battery applications, the energy densities of 274.9 Wh/kg in the half cell at 0.5 C for 100 cycles, after copper doping, which is higher than 252.7 Wh/kg for the prototype (Fig. S3 in Supporting information).

The galvanostatic charge/discharge and corresponding different capacity (dQ/dV) curves of NCM and other doped cathodes are characterized (Fig. S4 in Supporting information), which exhibits the voltage platform and reversible capacity at 0.5 C for 3rd, 5th, 10th, 50th and 100th cycles. Moreover, there are about five couples of redox peaks at around 2.0 V, 3.36/3.28 V, 3.57/3.44 V, 3.93/3.81 V in dQ/dV curves and CV curves (Figs. S4a-h and S5 in Supporting information), corresponding to the redox reactions of Mn^{4+}/Mn^{3+}, Co^{3+}/Co^{4+}, Ni^{2+}/Ni^{3+}, Ni^{3+}/Ni^{4+}couples, respectively [46]. The dQ/dV curves delivered that the enhancement of cycle performance was related to the increase of structural reversibility. The redox peaks around 2.0 V are gradually absent in $NCMTi_{0.02,}$ $NCMV_{0.02}$, $NCMCr_{0.02,}$ and $NCMZn_{0.02}$ samples indicating that Mn^{2+} is dissolved in the electrolyte [47]. The superstructure materials would result in cracks, interface instability, and further consumption of electrolytes thus presenting a larger polarization along with local inactivation while cycling, which is consistent with electrochemical performances [48]. In comparison with counterparts, doped samples exhibit smoother galvanostatic curves and lower peaks intensities (Figs. S4i-p in Supporting information), especially for the $NCMCu_{0.02}$ electrode also delivered less voltage decrease along with the rising of cycles, which demonstrates that ions doped (Sc^{3+}, Fe^{3+}, and Cu^{2+}) promote the disordering of Na^+/vacancies [49]. Meanwhile, the dQ/dV curves for 100 cycles present good coincidence and demonstrate that Cu^{2+} doped decrement lattice distortion of Mn^{3+} and thereby strengthening the reversibility.

Although the electrochemical performances are divergent, the refinement structure could reveal nuance (Figs. 2c-e). In P2-type materials, Na^+ could occupy two different types of trigonal pris-

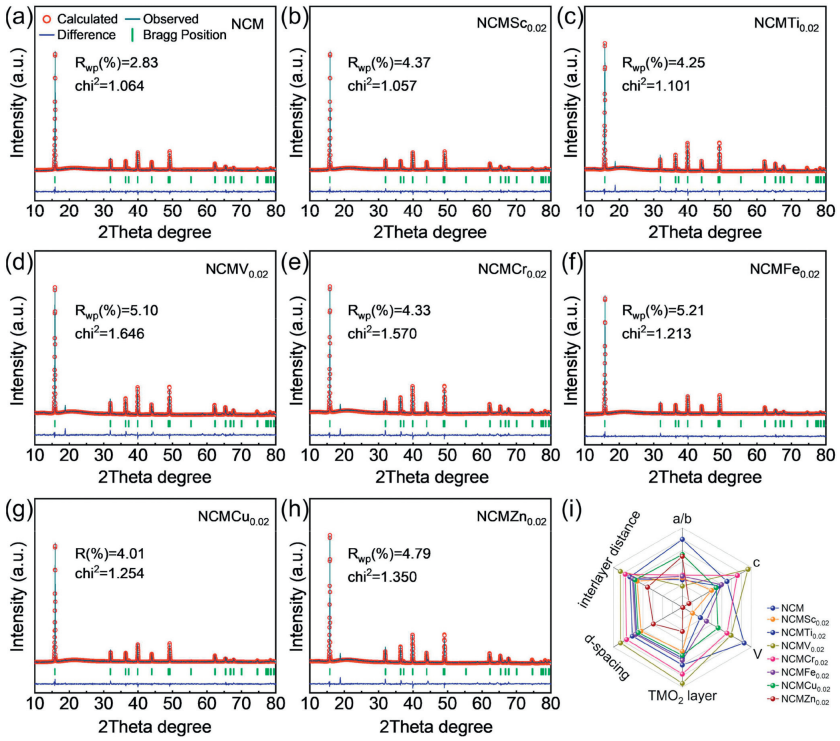

Fig. 1. The XRD patterns with corresponding Rietveld refinement plots of (a) NCM, (b) $NCMSc_{0.02}$, (c) $NCMTi_{0.02}$, (d) $NCMV_{0.02}$, (e) $NCMCr_{0.02}$, (f) $NCMFe_{0.02}$, (g) $NCMCu_{0.02}$ and (h) $NCMZn_{0.02}$ samples, respectively. (i) Comparison of refinement parameters for eight specimens.

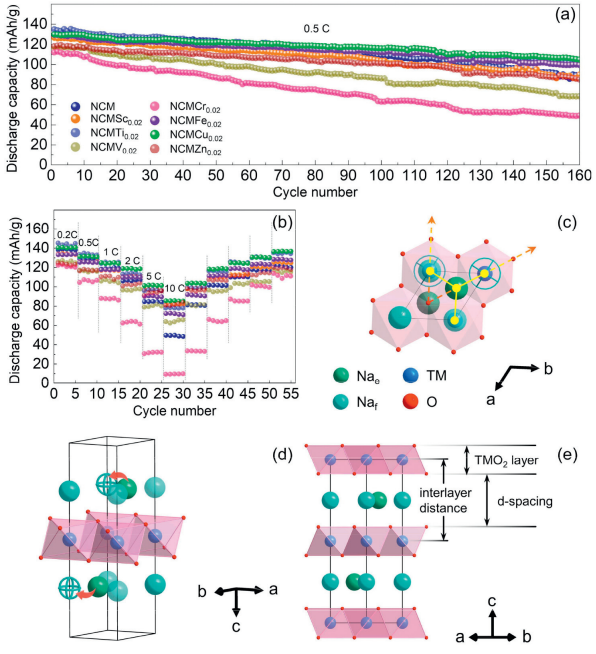

Fig. 2. (a) Cycling stability and (b) rate performances between 1.5 V and 4.2 V of NCM, $NCMSc_{0.02}$, $NCMTi_{0.02}$, $NCMV_{0.02}$, $NCMCr_{0.02}$, $NCMFe_{0.02}$, $NCMCu_{0.02}$ and $NCMZn_{0.02}$, respectively. (c-e) Schematic diagram of structures in various directions.

matic sites, where they either share faces (Na_f) or edges (Na_e) with TMO_6 octahedra because of the large Coulombic repulsion between the two adjacent Na^+ [50]. The Na^+ in the Na_e sites are usually *via* the Na_f site for extraction/insertion, the crystal structure thus suffers from a series of TMO_2 slabs gliding (uneven force along with the direction of the arrows) to form the octahedral site and stacking sequences of oxide layers (Figs. 2c-e) [51]. Nevertheless, the d-spacing, TMO_2 layer, as well as interlayer distance could help to research the interrelationships, which are contrasted in Table S3 (Supporting information). For example, the $NCMCu_{0.02}$ sample shows approximate TMO_2-layer yet larger d-spacing than $NCMSc_{0.02}$, while the $NCMCr_{0.02}$ and $NCMV_{0.02}$ samples show enlarged parameters due to the appearance of orthorhombic phase, which both agreed with former electrochemical performances. The results of the Rietveld refinements reveal that compressing the TMO_2 layer and interlayer distance in tandem with extending the *d*-spacing are rendered for a robust framework of P2-type structures and expedited diffusion channels, which is conducive to the extraction/embedding of Na^+, structure stability as well as improving electrochemical performances. From the above results, we have concluded that the relatively higher ion radius attained good structure configuration, while the lower valence state could change intermolecular interaction within interslabs facile Na^+ kinetics and enhanced the concentration of Mn^{4+} thus suppressing the cooperative Jahn-Teller distortion. Considering the phase composition, economic value, and research status, the NCM, $NCMSc_{0.02}$, $NCMFe_{0.02}$ and $NCMCu_{0.02}$ samples will be further discussed both from an electrochemical point of view and *in situ* XRD recorded during intercalation/deintercalation.

The micro-morphology and element distribution were investigated by SEM and EDS mapping. In Fig. S6 (Supporting information), the typical uniformly nanosheet structure with a thickness range of 12.4–15.7 nm was synthesized *via* co-precipitation, and a thinner primary nanosheet with dispersal distribution could be conducive to mixing between carbonates and transition metal during the sintering process. After sintering (Fig. S7 in Supporting information), all of the as-prepared four samples exhibit micro-scale bulk characteristics, especially for the $NCMCu_{0.02}$ sample, which is made up of a series of thinner nanosheets stacked on top of each other. The corresponding EDS mapping for doped samples indicates that the doped elements of Sc, Fe and Cu are uniformly dispersed within the sintered samples (Fig. S8 in Supporting information),

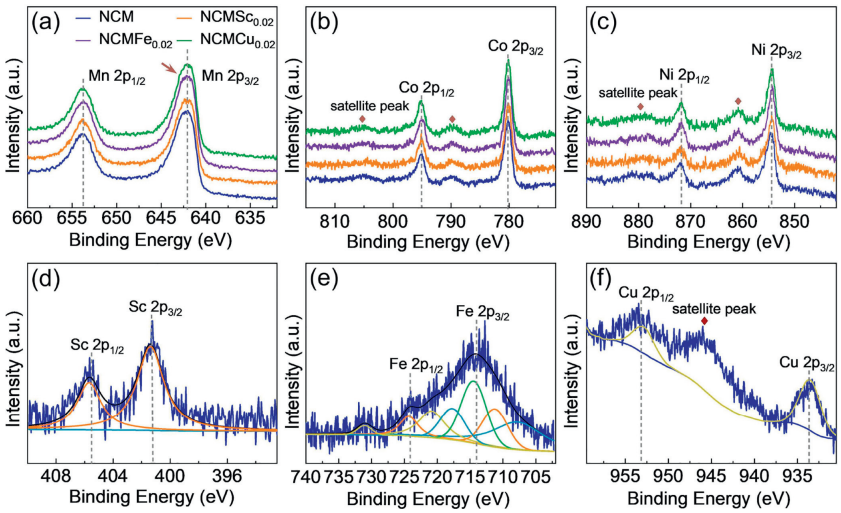

Fig. 3. XPS spectra of NCM, $NCMSc_{0.02}$, $NCMFe_{0.02}$ and $NCMCu_{0.02}$, respectively. (a) Mn 2p, (b) Co 2p, (c) Ni 2p, (d) *Sc* 2p, (e) Fe 2p and (f) Cu 2p.

confirming that the Sc^{3+}, Fe^{3+} and Cu^{2+} remained. TEM measurement was carried out to further confirm the lattice structure and micro-morphology, which displays a series of stacked structures with a side length of 1–3 μm in Figs. S7a_1-d_1. The d-spacing between the neighboring lattice fringes of four samples is about 0.25 nm and 0.56 nm, matching with the (100) and (002) planes of the P63/mmc space group. Meanwhile, the single P2 phase with a typical hexagonal lattice pattern is confirmed by SAED images, clearly showing the high ordering of the atomic arrangement, in which accordance with the XRD results.

In order to verify the participation of transition metal elements and corresponding valences for four samples, the XPS analyses were performed (Fig. 3). It can be seen that all samples possess a similar survey spectrum (Fig. S9 in Supporting information). Two main peaks are located at ~642.1 eV and ~653.5 eV, indicating that Mn^{4+} and Mn^{3+} coexist in all samples (Fig. 3a) [52]. As compared with others, the feature of the slight split in Mn $2p_{3/2}$ peak of the $NCMCu_{0.02}$ sample also demonstrates that more Mn^{4+} have existed after Cu^{2+} doped, which is beneficial for mitigating the Jahn-Teller effect and rendered for the stabilization of non-distortion P2 hexagonal crystal structure. The Co $2p_{1/2}$ peak at ~795.4 eV and Co $2p_{3/2}$ peak at ~780.4 eV as well as their corresponding satellite peaks can be ascribed to Co^{3+} and Co^{2+}, respectively (Fig. 3b) [53]. The Ni 2p peak can be separated into four peaks, in which two distinct peaks appearing at ~872.1 eV and ~854.9 eV can be assigned to Ni $2p_{1/2}$ and Ni $2p_{3/2}$ respectively, another two satellite peaks also confirmed the existence of Ni^{2+} (Fig. 3c) [54]. The Ni^{2+} and Mn^{4+} are the Jahn-Teller inactive centers resulting in highly symmetric and stable crystal structures [55]. Moreover, the oxidation states of dopants are present in Figs. 3d-f. The peaks of Sc $2p_{1/2}$ (401.8 eV) and Sc $2p_{3/2}$ (405.7 eV) are assigned to Sc^{3+} [40]. By using a Gaussian fitting method, Fe 2p spectra can be assigned to the existence of Fe^{3+} [56]. The binding energies of 933.6 eV and 953.2 eV with corresponding satellite peaks have also confirmed the valence of Cu is +2 [57].

Nyquist plots of four cathodes and corresponding fitting results *via* equivalent circuits were compared (Fig. S10 and Table S4 in Supporting information). The R_s was the internal resistance, CPE and R_{ct} are the double-layer capacitance and charge transfer resistance as well as R_f is regarded as the film resistance. The results of the $NCMCu_{0.02}$ electrode exhibit R_s and R_{ct} are 1.911 and 212.9 Ω, lower than other electrodes, indicating much faster kinetic and smaller polarization of Cu^{2+} doped cathode owing to the lighten of Na^+/vacancy ordering.

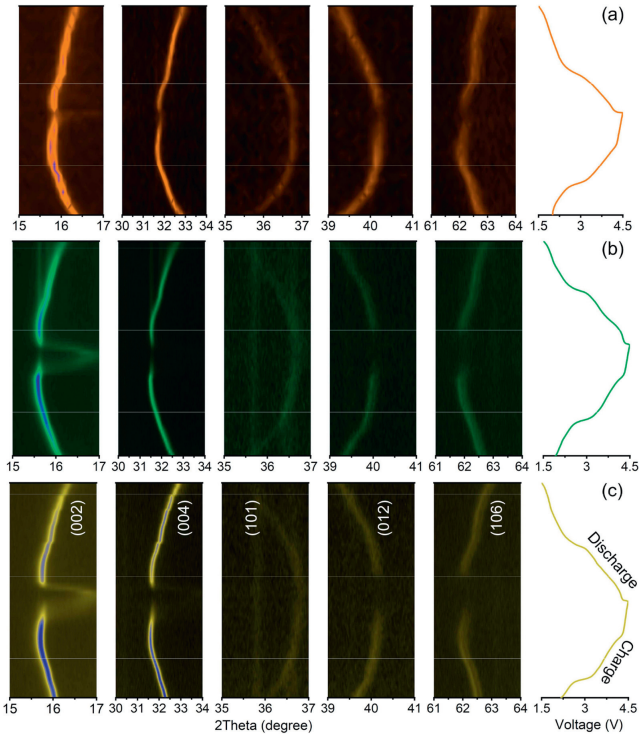

Fig. 4. The diffraction peaks of (002), (004), (101), (012) and (106) form operando XRD patterns of layered P2 phase during 1st cycle with corresponding galvanostatic charge/discharge curves at 0.1C for $NCMSc_{0.02}$, $NCMFe_{0.02}$ and $NCMCu_{0.02}$ electrodes, respectively.

To obtain deeper insights into the structural evolution and behaviors of doped ions, operando XRD tests were carried out for $NCMSc_{0.02}$, $NCMFe_{0.02}$ and $NCMCu_{0.02}$ electrodes in the voltage of 1.5–4.5 V at 0.1 C. It can be seen from Fig. 4, all the samples exhibited the same trend of voltage platform upper 4.3 V and continuous peak shifts of the (002) and (004) diffraction peaks toward the lower angle. The results reveal that either interlayer distance along the c-axis is enlarged or compressed during Na^+ extraction or insertion, which is owing to strengthened O–O electrostatic repulsion between the adjacent TMO_2 layer. Besides, the (101), (106) as well as (012) peaks shift toward higher angles due to the redox reactions of TM ions upon desodiation to form high-valence

ions with smaller ionic radii. Upon Na^+ intercalation, the structures almost follow a similar reverse evolution, contributing to the high reversibility of the structure for doped samples. According to Bragg's Law and refinement results, Cu^{2+} doped cathode delivered the modified distance in *d*-spacing and TMO_2 layer (along the c-axis) than the counterparts, which not only facilitate Na^+ migrations from Na_e and Na_f position in the P2 phase but also synergistic alleviate the slab slide. The phenomena in operando XRD results are consistent with the theoretical calculations of TMO_2 layer, d-spacing, and interlayer distance by Rietveld refinements. The widened interlayer spacing could optimize and improve stability in the cathode structures, ultimately leading to the improvement of the electrochemical performances.

In summary, a series of hierarchical cathode materials were obtained by doping periodic elements such as Sc, Ti, V, Cr, Fe, Cu and Zn into the NCM by a facile sintered method. The results of operando XRD at high voltage (4.5 V) and Rietveld refinements delivered the collaborative strategy among the compressed TMO_2 layer, enlarged-spacing, as well as the changes of interlayer distance, which are closely related to the radii and valence states. Intermingle redox active metal ions (Sc^{3+}, Fe^{3+} and Cu^{2+}) into the TM sites could subdue the Na^+/vacancy ordering and repress the expansion of the c axis during insertion/extraction, where the $NCMCu_{0.02}$ contained a higher ion radius and lower valence could further tune up the valence state of TM layers shows the best electrochemical performance. The fitted smaller R_s and R_{ct} *via* EIS test for $NCMCu_{0.02}$ also can expedite Na^+ migration and heighten the high rate capability. This work provides a strategy to design higher energy densities for reversible cathode materials in SIBs.

Declaration of competing interest

The authors report no declarations of interest.

Acknowledgments

This work was financially supported by the National Natural Science Foundation of China (Nos. 52263010, 51902090), Henan Key Research Project Plan for Higher Education Institutions (No. 23A150038), 2023 Introduction of studying abroad talent program, "111" Project (No. D17007), Henan Provincial Key Scientific Research Project of Colleges and Universities (No. 23A150038), Key Scientific Research Project of Education Department of Henan Province (No. 22A150042), the National students' platform for innovation and entrepreneurship training program (No. 201910476010), the China Postdoctoral Science Foundation (No. 2019 M652546), and the Henan Province Postdoctoral Start-Up Foundation (No. 1901017).

Supplementary materials

Supplementary material associated with this article can be found, in the online version, at doi:10.1016/j.cclet.2023.108810.

References

[1] Q. Liu, Z. Hu, M. Chen, et al., Adv. Funct. Mater. 30 (2020) 1909530.
[2] Q. Bai, L.F. Yang, H.L. Chen, et al., Adv. Energy Mater. 8 (2018) 1702998.
[3] R. Usiskin, Y. Lu, J. Popovic, et al., Nat. Rev. Mater. 6 (2021) 1020–1035.
[4] C. Li, B. Liu, N. Jiang, et al., Nano Res. Energy 1 (2022) e9120031.
[5] Q. Liu, Y. Hu, X. Yu, et al., Nano Res. Energy 1 (2022) e9120037.
[6] C. Delmas, C. Fouassier, P. Hagenmuller, Phys. B+C 99 (1980) 81–85.
[7] C. Zhao, Q. Wang, Z. Yao, et al., Science 370 (2020) 708–711.
[8] T. Or, S.W.D. Gourley, K. Kaliyappan, et al., Electrochem. Energy R 5 (2022) 20.
[9] Q.Y. Shen, Y.C. Liu, L.F. Jiao, et al., Energy Storage Mater. 35 (2021) 400–430.
[10] X. Li, Y. Wang, D. Wu, et al., Chem. Mater. 28 (2016) 6575–6583.
[11] A. Gutierrez, W.M. Dose, O. Borkiewicz, et al., J. Phys. Chem. C 122 (2018) 23251–23260.
[12] J. Billaud, R.J. Clement, A.R. Armstrong, et al., J. Am. Chem. Soc. 136 (2014) 17243–17248.
[13] Z.Y. Li, X.B. Ma, H. Guo, et al., ACS Appl. Energy Mater. 4 (2021) 5687–5696.
[14] J.Y. Jiao, K. Wu, R.B. Dang, et al., Electrochim. Acta 384 (2021) 138362.
[15] R. Qi, M.H. Chu, W.U. Zhao, et al., Nano Energy 88 (2021) 106206.
[16] H.V. Ramasamy, K. Kaliyappan, R. Thangavel, et al., J. Mater. Chem. A 5 (2017) 8408–8415.
[17] Q.C. Wang, Z. Shadike, X.L. Li, et al., Adv. Energy Mater. 11 (2021) 2003455.
[18] X.L. Li, T. Wang, Y.F. Yuan, et al., Adv. Mater. 33 (2021) 2008194.
[19] Y.C. Liu, Q.Y. Shen, X.D. Zhao, et al., Adv. Funct. Mater. 30 (2020) 1907837.
[20] H. Zhao, J. Zhong, Y. Qi, et al., Chem. Eng. J. 465 (2023) 143032.
[21] P. Wei, X.P. Sun, Z.M. He, et al., Fuel 339 (2023) 127303.
[22] W.H. Zuo, X.S. Liu, J.M. Qiu, et al., Nat. Commun. 12 (2021) 4903.
[23] Z.B. Liu, J.D. Shen, S.H. Feng, et al., Angew. Chem. Int. Ed. 60 (2021) 20960–20969.
[24] J.T. Jin, Y.C. Liu, Q.Y. Shen, et al., Adv. Funct. Mater. 32 (2022) 2203424.
[25] J.T. Jin, Y.C. Liu, X.D. Zhao, et al., Angew. Chem. Int. Ed. 62 (2023) e202219230.
[26] K. Liu, S. Tan, J. Moon, et al., Adv. Energy. Mater. 10 (2020) 2000135.
[27] C. Vaalma, D. Buchholz, S. Passerini, J. Power Sources 364 (2017) 33–40.
[28] L.T. Yang, L.Y. Kuo, J.M.L. del Amo, et al., Adv. Funct. Mater. 31 (2021) 2102939.
[29] D.M. Dai, J.X. Qiu, H.Y. Hou, et al., J. Mater. Chem. A 9 (2021) 18272–18279.
[30] E.N. Bassey, P.J. Reeves, M.A. Jones, et al., Chem. Mater. 33 (2021) 4890–4906.
[31] Q.Y. Shen, Y.C. Liu, X.D. Zhao, et al., Adv. Funct. Mater. 31 (2021) 2106923.
[32] K. Kannan, M. Kouthaman, P. Arjunan, et al., Inorg. Chem. Commun. 124 (2021) 108383.
[33] X. Liu, W. Zuo, B. Zheng, et al., Angew. Chem. Int. Ed. 58 (2019) 18086–18095.
[34] L. Wang, Y. Wang, X. Yang, et al., J. Mater. Sci. 54 (2019) 12723–12736.
[35] X.H. Yang, Y.Z. Wang, J.L. Wang, et al., J. Phys. Chem. Solids 148 (2021) 109750.
[36] L. Wang, Y. Wang, J. Zhao, et al., Ionics 25 (2019) 4775–4786.
[37] L. Zhang, C.C. Wang, Y.C. Liu, et al., Chem. Eng. J. 426 (2021) 130813.
[38] K. Liang, H. Zhao, J. Li, et al., Small 19 (2023) 2207562.
[39] K. Liang, H.S. Zhao, J.B. Li, et al., Appl. Surf. Sci. 615 (2023) 156412.
[40] S. Bhuvaneswari, U.V. Varadaraju, R. Gopalan, et al., Electrochim. Acta 301 (2019) 342–351.
[41] J. Xia, N. Zhang, Y. Yang, et al., Adv. Funct. Mater. 33 (2023) 2212869.
[42] M. Guignard, C. Didier, J. Darriet, et al., Nat. Mater. 12 (2013) 74–80.
[43] B. Toby, J. Appl. Crystallogr. 34 (2001) 210–213.
[44] B. Toby, J. Appl. Crystallogr. 38 (2005) 1040–1041.
[45] P.F. Wang, H.R. Yao, X.Y. Liu, et al., Adv. Mater. 29 (2017) 1700210.
[46] B.E. Conway, V. Birss, J. Wojtowicz, J. Power Sources 66 (1997) 1–14.
[47] C. Zhan, T. Wu, J. Lu, et al., Energ. Environ. Sci. 11 (2018) 243–257.
[48] S. Huo, L. Sheng, W. Xue, et al., Adv. Energy Mater. 13 (2023) 2204343.
[49] Q.J. Mao, Y. Yu, J.K. Wang, et al., J. Mater. Chem. A 9 (2021) 10803–10811.
[50] D. Carlier, J.H. Cheng, R. Berthelot, et al., Dalton Trans. 40 (2011) 9306–9312.
[51] C. Delmas, Mater. Res. Bull. 17 (1982) 117.
[52] Y.M. Zheng, X.B. Huang, X.M. Meng, et al., ACS Appl. Mater. Inter. 13 (2021) 45528–45537.
[53] Q. Huang, P.G. He, L. Xiao, et al., ACS Appl. Mater. Inter. 12 (2020) 2191–2198.
[54] Q.Q. Zhao, F.K. Butt, M. Yang, et al., Energy Storage Mater. 41 (2021) 581–587.
[55] P.F. Wang, Y. You, Y.X. Yin, et al., Adv. Energy Mater. 8 (2018) 1701912.
[56] J.K. Park, G.G. Park, H.H. Kwak, et al., ACS Omega 3 (2018) 361–368.
[57] J. Wang, H. Liu, Q. Yang, et al., ACS Appl. Mater. Inter. 12 (2020) 34848–34857.